

4

INTEGRAL EQUATIONS

As standard microelectronic technology approaches fundamental limitations in speed and power consumption, novel computing strategies are strongly needed. Analog optical computing enables processing large amounts of data at a negligible energy cost and high speeds. Based on these principles, ultra-thin optical metasurfaces have been explored to process large images in real-time, in particular for edge detection.

Within this chapter, an ultra-thin Si metasurface-based platform for analog computing that is able to solve Fredholm integral equations of the second kind using free-space visible radiation is presented. A Si-based metagrating was inverse-designed to implement the scattering matrix synthesizing a prescribed Kernel corresponding to the mathematical problem of interest. Next, a semi-transparent mirror was incorporated into the sample to provide adequate feedback and thus perform the required Neumann series solving the corresponding equation in the analog domain at the speed of light. Visible wavelength operation enables a highly compact, ultra-thin device that can be interrogated from free space, implying high processing speeds and the possibility of on-chip integration.

4.1. THEORY AND DESIGN

THE idea of using light to outsource specific computing tasks comes with several advantages. First, there is a clear enhancement in processing speeds as the computation is performed at the speed of light traveling through metamaterials with typical sizes smaller than or comparable to the wavelength of operation. Also, processing signals in the optical domain enables massive parallelization and may potentially avoid unnecessary analog-to-digital conversion. As shown in the previous chapters, several image processing tasks can be performed before the image is discretized into pixels, relying on the possibility of engineering the angular response of metasurfaces and hence impart instantaneously a mathematical operation to the spatial content of an input signal. Finally, analog computing meta-devices can be passive, implying an extremely low energy usage.

4

A key question is whether it is possible to go beyond simple image processing tasks and focus on a more complex mathematical problem, such as solving a linear integral equation. The latter is an equation containing the unknown function within an integral and can be categorized in two ways:

- If the limits of integration $[a, b]$ are fixed, the equation is labeled as *Fredholm* equation, otherwise it is a *Volterra* equation. The following is an example of a Volterra equation:

$$g(u) = f(u) + \int_a^u K(u, v)g(v)dv \quad (4.1)$$

- If the unknown function appears only under the integral sign, the equation is labeled as *first kind*. If it appears both inside and outside the integral, it is labeled *second kind*. As an example, this is a Fredholm equation of the first kind:

$$f(u) = \int_a^b K(u, v)g(v)dv \quad (4.2)$$

In the examples presented, $g(u)$ is the unknown function that the equation has to be solved for, while the known function of two variables $K(u, v)$ is called *kernel*. The extra function $f(u)$ is also assumed to be known. If $f(u) = 0$, the equation is said to be homogeneous.

Integral equations are present in several scientific fields, for example, scattering (e.g. quantum theory of scattering by a potential [1]) and transport phenomena. Moreover, it is more convenient to recast some specific problems described by differential equations with boundary conditions into integral equations [2]. Furthermore, as it will be clear later, the platform presented here allows mapping of discretized arbitrary linear operators and inversion of those. Hence, it is applicable to any generic linear inverse problem.

The concept of a wave-based integral equation solver has been recently demonstrated in the microwave regime for symmetric and non-symmetric kernels and in a multi-frequency parallel fashion [3, 4], but relying on guided waves in bulky metamaterial setups. An important next challenge is to demonstrate if such a complex mathematical operation can be carried out in the optical spectral range, ideally within an ultrathin form factor that can be interrogated through free-space radiation. This will enable the fabrication of far more compact on-chip devices operated at wavelengths that

are widely used for communication technology. This dramatic size reduction further implies a drastic increase in processing speeds as light has to travel much shorter distances. Here, we demonstrate a Si metasurface-based optical platform that combines a tailored scattering matrix design and a feedback system to enable the solution of Fredholm integral equations of the second kind from the far-field

$$g(u) = I_{\text{in}}(u) + \int_a^b K(u, v)g(v)dv \quad (4.3)$$

where $g(u)$ is the unknown solution of Eq.(4.3), $K(u, v)$ is the kernel of the integral operator, and $I_{\text{in}}(u)$ is an arbitrary input function. Mathematically, this form of equation may be analytically solvable if it is in separable form or for some special kernels, and an inversion formula may exist (e.g., a Fourier transform). However, when certain convergence conditions for the kernels are satisfied a general technique to solve Eq.(4.3) is to exploit the Neumann successive approximation method: we assume an initial guess $g_0(u) = I_{\text{in}}(u)$ and successive approximations can be obtained by evaluating $g_{i+1}(u) = I_{\text{in}}(u) + \int_a^b K(u, v)g_i(v)dv$, whereupon eventually $g_n(u)$ converges to the solution $g(u)$ as $n \rightarrow \infty$ [2]. Here, we show how to physically implement this iterative procedure in an analog fashion employing a Si metasurface coupled to a feedback system.

First, Eq.(4.3) is discretized by sampling its independent variables, u and v , over N points in the interval $[a, b]$ to form two vectors with such variables \mathbf{u} and \mathbf{v} . The application of the integral operator $\int_a^b K(u, v)[\cdot]dv$ on the function $g(u)$ is then analogous to the multiplication (or application) of a matrix operator $\mathbf{K} = K(\mathbf{u}, \mathbf{v})\frac{a-b}{N}$ on a vector $\mathbf{g} = g(\mathbf{u})$. Thus, Eq.(4.3) may be numerically approximated by the $N \times N$ matrix equation

$$\mathbf{g} = \mathbf{I}_{\text{in}} + \mathbf{K}\mathbf{g} \quad (4.4)$$

Second, the solution \mathbf{g} is represented as a Neumann series

$$\mathbf{g} = \sum_i (\mathbf{K})^i \mathbf{I}_{\text{in}} + = (\mathbb{I}_N - \mathbf{K})^{-1} \quad (4.5)$$

where \mathbb{I}_N is the $N \times N$ identity matrix. The convergence of the Neumann series demonstrates that the inverse operator $(\mathbb{I}_N - \mathbf{K})$ exists. Next, it is possible to think of the N mathematical sampling points as N discrete physical modes, and thus \mathbf{g} is a vector representing the complex amplitude of these modes on a given plane with a chosen direction. The integral operator can then be represented by a scattering matrix that performs matrix multiplication between these sets of modes.

If we consider a periodic metagrating, the input/output modes can be mapped into the N discrete diffraction channels determined by the periodicity and the wavelength, while the discretized integral operator \mathbf{K} can be mapped onto the metasurface scattering matrix \mathbf{S} that governs the coupling between these channels.

Following the schematics in Fig. 4.1, the discretized input \mathbf{I}_{in} is a vector of length N containing the complex amplitudes of the plane waves addressing the system via its available diffraction channels, acting as seed guess $\mathbf{g}_0 = \mathbf{I}_{\text{in}}$. The vector is multiplied by the metasurface scattering matrix upon its first reflection, resulting in a more refined

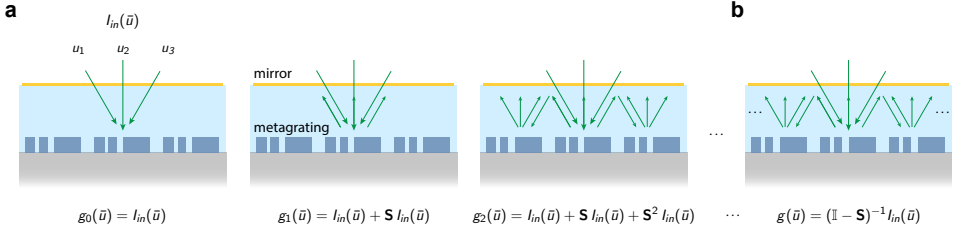


Figure 4.1: An input vector \mathbf{I}_{in} is fed to the system in the form of N plane waves with different complex amplitudes incident along N diffraction channels. The signal interacts repeatedly with a metagrating bouncing back from a partially reflecting mirror, each time multiplied by the metagrating scattering matrix and therefore building up the terms of a Neumann series of subsequent matrix multiplications required for solving the integral equation. For the sake of simplicity, the formulas underneath the panels do not take into account the semi-transparent mirror scattering matrix at this stage.

4

guess \mathbf{g}_1 to the solution of the integral equation associated with \mathbf{K} . The signal is then reflected by a semitransparent mirror and fed back to the grating for the next iteration. Intuitively, the system performs an analog Neumann series operation at the speed of light by iteratively applying the \mathbf{S} matrix on the seed vector through multiple reflections, in the same way the mathematical integral operator is applied repeatedly on the initial guess function.

The entire computing metastructure is therefore composed of two elements: (1) a metagrating with a period that determines the number of input-output modes (grating orders), and unit cell with tailored geometry defining the scattering matrix of interest, (2) a semi-transparent mirror enabling feedback and in-coupling combined with a spacer layer.

4.1.1. KERNEL DESIGN

At the foundations of the analogy between the integral equation solving and the behavior of an optimized periodic metagrating coupled to a feedback lies the requirement of designing the \mathbf{S} -matrix of a periodic structure by setting its periodicity (i.e., the number of input/output modes and hence the dimension of the \mathbf{S} -matrix) and optimizing its unit cell (i.e., optimize the coupling of light into the defined diffraction modes in amplitude and phase).

First, we set the periodicities p and w of the grating (Fig. 4.2a) to have three diffraction orders in reflection at the target wavelength $\lambda_0 = 706$ nm. We choose this wavelength because it is still within the visible spectral range while Si losses are less severe, light sources in this spectral range are readily accessible, and the corresponding sub-micron unit cell footprint enables compact circuit design and integration. Specifically, we choose $w = 825$ nm while the orthogonal periodicity $w = 400$ nm is set to be sub-wavelength. This enhances the degrees of freedom for the unit cell design without opening additional diffraction channels. Hence, the system is addressed by six ports corresponding to six different diffraction channels (Fig. 4.2b) at angles $\theta_0 = \sin^{-1}(\lambda_0/p n_{\text{sup}})$, $\theta_T = \sin^{-1}(\lambda_0/p n_{\text{sub}})$ where n_{sup} , n_{sub} are the superstrate (SiO_2) and substrate (Al_2O_3) refractive indices respectively.

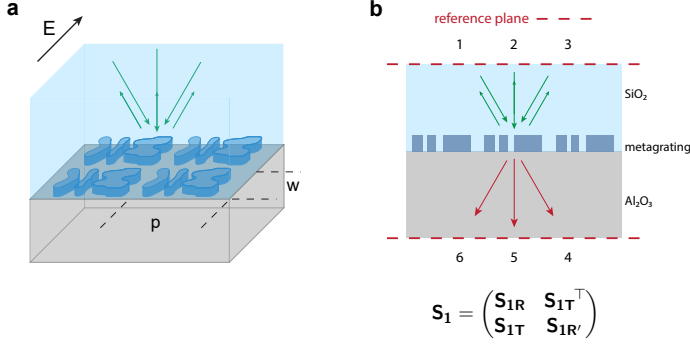


Figure 4.2: **a** Schematic illustration of a 2D metagrating (periodicities p and w) with a suitably engineered unit cell geometry. The black arrow indicates the polarization (TE) of the incoming E field. **b** Schematics of the input and output ports including the related reference planes for the metagrating and corresponding S-matrix.

The plane waves probing the system via these diffraction channels are TE polarized and the linear relationship between these incident, transmitted, and reflected waves defines the scattering matrix of the system. The s-parameters defining this matrix are complex numbers normalized such that $|S_{ij}|^2$ is the transmittance to port i when port j is illuminated (taking into account refractive indices and angles)

$$S_1 = \begin{pmatrix} S_{1R} & S_{1T}^T \\ S_{1T} & S_{1R'} \end{pmatrix} = \begin{pmatrix} r_{11} & r_{12} & r_{13} & t_{14} & t_{15} & t_{16} \\ r_{21} & r_{22} & r_{23} & t_{24} & t_{25} & t_{26} \\ r_{31} & r_{32} & r_{33} & t_{34} & t_{35} & t_{36} \\ t_{41} & t_{42} & t_{43} & r_{44} & r_{45} & r_{46} \\ t_{51} & t_{52} & t_{53} & r_{54} & r_{55} & r_{56} \\ t_{61} & t_{62} & t_{63} & r_{64} & r_{65} & r_{66} \end{pmatrix} \quad (4.6)$$

where S_{1R} and S_{1T} are the reflection and transmission sub-blocks. Since the Neumann series is performed in reflection, only the reflection sub-block S_{1R} needs to be designed: it contains the complex reflection coefficients connecting the diffraction channels in the spacer layer above the metagrating. It is important to stress that the choice of working with the reflective part of the s-matrix allows for a configuration that is easier to fabricate experimentally but limits the generality of the kernels that can be implemented to symmetric ones. However, these concepts may be extended to more general kernels by optimizing the transmissive block of the s-matrix and with an appropriate feedback system.

To prove the generality of our approach, we began our problem by choosing a random passive and reciprocal (i.e., symmetric) matrix with $N = 3$

$$S_{1R} = \begin{pmatrix} 0.239 + 0.052i & -0.233 - 0.083i & 0.246 + 0.329i \\ -0.233 - 0.083i & -0.381 - 0.514i & 0.339 - 0.262i \\ 0.246 + 0.329i & 0.339 - 0.262i & -0.314 + 0.156i \end{pmatrix}. \quad (4.7)$$

Inverse design techniques [5–10] were utilized in order to create a design that satisfies the 9 constraints contained within S_{1R} . Specifically, the grating unit cell topology is

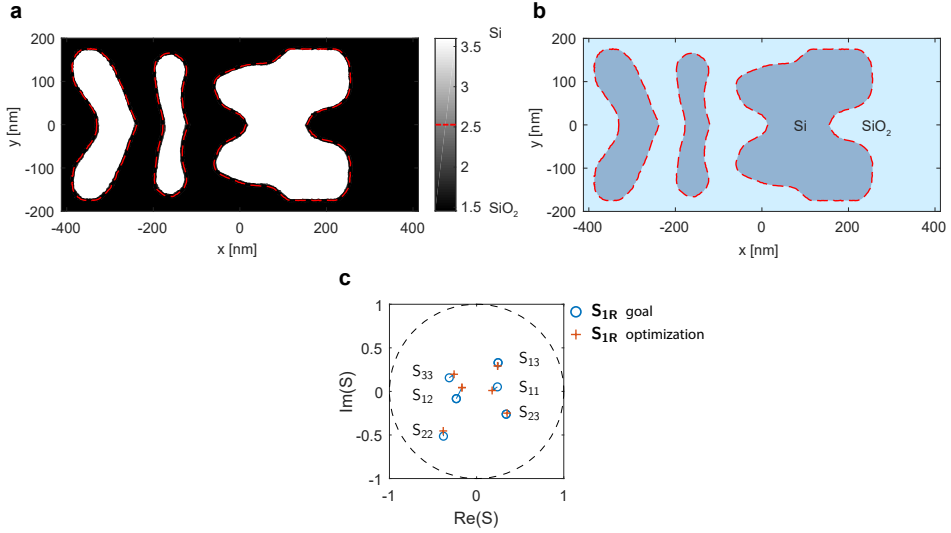


Figure 4.3: **a** Optimized unit cell refractive index distribution (gray-scale). Black indicates the refractive index of SiO₂ while white indicates that of Si. The colormap is continuous even if it appears binarized. The red dashed line indicated the contour used to generate the final unit cell. **b** Binarized metagrating unit-cell made of silicon (blue) and SiO₂ (light blue). **c** Simulation results for the S_{1R} matrix elements of the inverse-designed metagrating (orange crosses) and the corresponding desired matrix elements (blue circles).

optimized employing COMSOL Multiphysics's optimization module while the height h of the etched silicon unit cell is set to 150 nm. The figure-of-merit to be minimized during the optimization is the sum of the squared “distances” on the complex plane between the complex-valued matrix elements of the S matrix of a designed geometry and the prescribed ones in Eq.(4.7), $FOM = \sum_{i,j} |S_{1Rij} - S_{1R-optij}|^2$. Also, polarization conversion is minimized as it would open extra channels effectively changing the dimension of S_1 . During the optimization, the unit cell permittivity distribution (Fig. 4.3a) is periodically blurred to avoid small features that are hard to fabricate and a soft step function is applied to drive the optimum toward a more binary configuration. Also, the mesh size was reduced along the iterations to increase the accuracy of the simulation. Once the desired figure of merit is reached for an experimentally feasible unit cell, the permittivity distribution is fully binarized: all the domains with a refractive index below and above the threshold $(n_{Si} + n_{SiO_2})/2 \approx 2.6$ are converted to SiO₂ and Si respectively, therefore obtaining the final unit cell design (Fig. 4.3b). Furthermore, by changing the latter threshold, it is possible to generate expanded and eroded designs that are used to study the design tolerance to fabrication imperfections.

As shown in (Fig. 4.3d), the optimized metagrating approximates very well the desired S matrix, achieving a figure of merit as low as 0.058. This demonstrates that it is possible to inverse-design metagratings with a prescribed S-matrix, showing the feasibility of this optical computing concept for the solution of integral equations with a wide range of kernels.

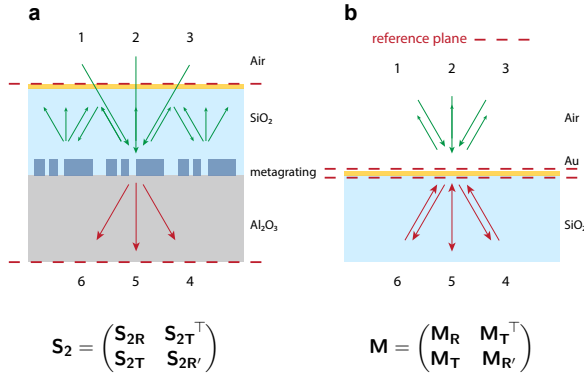


Figure 4.4: Schematics of the input and output ports including the related reference planes for **a** entire metastructure and **b** semi-transparent mirror. The corresponding S-matrix is underneath each panel.

4.1.2. MATRIX INVERSION

What is discussed so far concerns only the design of the metagrating scattering matrix mapping the discretized integral Kernel operator K in Eq.(4.4). Next, to find the solution of the integral equation it is crucial to have a feedback system that repeatedly returns the signal reflected from the metagrating back to it, so that the Neumann series is constructed. To this end, the SiO_2 spacer is covered with a 15 nm thick Au layer to form a semitransparent mirror [11]. The distance between the metagrating and mirror is $487 \text{ nm} \approx \lambda_0/n_{\text{SiO}_2}$ to avoid near-field coupling, which may introduce additional modes into the system. The S matrix characterizing the mirror is

$$M = \begin{pmatrix} M_R & M_T^T \\ M_T & M_{R'} \end{pmatrix} \quad (4.8)$$

where $M_{R'}$ is the sub-block representing reflection from the SiO_2 side and M_T is its transmission counterpart. Including the mirror, the scattering matrix of the entire metastructure (grating, SiO_2 spacer, and mirror) becomes

$$S_2 = \begin{pmatrix} S_{2R} & S_{2T}^T \\ S_{2T} & S_{2R'} \end{pmatrix}. \quad (4.9)$$

The Neumann series, and thus the solution of Eq.(4.4), is embedded in S_2 . The transmission of the entire stack, as measured in our experiment, is composed of a sum of terms each corresponding to an increasing number of interactions with the metagrating (see figs. 4.5a, 4.1) [12]:

$$S_{2T} = S_{1T}M_T + S_{1T}M_{R'}S_{1R}M_T + S_{1T}(M_{R'}S_{1R})^2M_T + \dots = S_{1T}(\mathbb{1}_3 - M_{R'}S_{1R})^{-1}M_T. \quad (4.10)$$

The transmission sub-block S_{2T} is composed of the inverse operator $(\mathbb{1}_3 - M_{R'}S_{1R})^{-1}$ solving Eq.(4.4) multiplied by the mirror transmission M_T and by the metasurface transmission S_{1T} . In other words, light is coupled into the system passing through the mirror first, and then the solution is outcoupled via the metasurface. Hence, to extract the solution computed by the metastructure, i.e. the linear combination of complex amplitudes

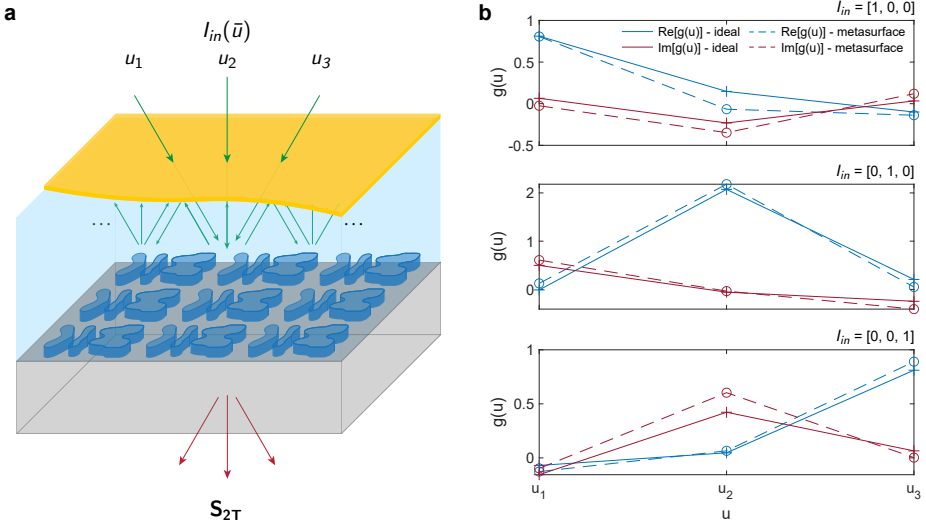


Figure 4.5: **a** The solution of Eq.(4.4) is built up inside the spacer layer in the form of a collection of complex wave amplitudes, one for each discrete diffraction channel. The solution is outcoupled and read out in transmission. **b** Analog solution (real and imaginary parts) of the integral equation (dashed line) obtained from the simulation results for the metastructure transmission, compared with the ideal theoretical solution $\mathbf{g} = (\mathbb{I}_N - \mathbf{K})^{-1}$ (solid lines), for the three orthogonal input vectors $(1, 0, 0)^\top$, $(0, 1, 0)^\top$, $(0, 0, 1)^\top$. The wavelength of operation in this simulation is $\lambda_0 = 706$ nm.

of the diffracted modes inside the spacer layer that converges after multiple passes, \mathbf{M}_\top and $\mathbf{S}_{1\top}$ must be de-embedded from $\mathbf{S}_{2\top}$.

Figure 4.5b compares the solution $\mathbf{M}_\top^{-1} \mathbf{S}_{2\top} \mathbf{S}_{1\top}^{-1}$ provided by the simulated metasurface transmission to the ideal solution of Eq.(4.4) with $\mathbf{K} = \mathbf{M}_R \mathbf{S}_{1R}$ and \mathbf{I}_{in} equal to the vectors belonging to the canonical basis generating the space of all possible input vectors (i.e., $(1, 0, 0)^\top$, $(0, 1, 0)^\top$, $(0, 0, 1)^\top$). Any input vector can be expressed as a linear combination of these, and given the linearity of the metasurface, agreement in the response for these basic excitations ensures that the structure can solve the integral equation problem for arbitrary inputs. The metasurface-based analog solution and the ideal solution show good agreement for all the inputs, both in terms of the real and imaginary part. Minor discrepancies are ascribed to the small difference between the desired \mathbf{S} matrix and the optimized one (see Fig. 4.3c) and this result demonstrates that it is possible to design the desired kernel \mathbf{K} and invert $(\mathbb{I}_3 - \mathbf{K})$ in a fully analog fashion.

4.2. EXPERIMENT

In this section, the experimental implementation of the all-optical integral equation solving metasurface is described in detail.

4.2.1. FABRICATION

The following fabrication steps were performed to obtain the optimized geometry analyzed in the previous section (see Fig. 4.6):

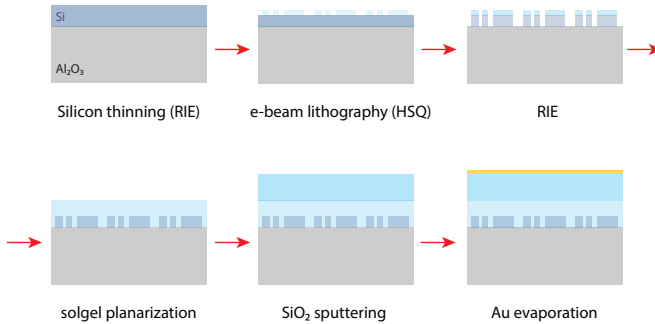


Figure 4.6: Schematics of the fabrication steps needed for the entire metastructure.

- c-Si on Al₂O₃ substrates were acquired from MTI corp. The c-Si (orientation: (100)) layer is 500 nm-thick, polished (surface roughness $R_q < 2.5$ nm) and undoped. The sapphire (orientation: R -plane) substrate is 0.46 mm-thick and double-side polished (surface roughness < 0.3 nm on the front side and optical grade polish on the back). The substrate was cleaned in base piranha, and the c-Si was etched to the final metasurface thickness ($h = 150$ nm) via reactive ion etching (RIE) employing CHF₃, SF₆, and O₂. The c-Si film thickness was checked with Filmetrics F20.
- After an O₂ plasma surface treatment a 50 nm thick layer of HSQ (hydrogen silsesquioxane) negative-tone resist was spin-coated and baked for 2 min at 180°C.
- The metasurface was patterned in the HSQ layer by exposure using a Raith Voyager e-beam lithography system (50 kV, dose 2300 $\mu\text{C}/\text{cm}^2$) and development in TMAH (Tetramethylammonium hydroxide) for 60 s at 50°C. As explained in Section 2.5 the pattern has to be aligned along the optical axis of sapphire during e-beam exposure.
- The pattern was then transferred into the c-Si by a two-step RIE (Reactive Ion Etching) process employing Cl₂, HBr, and O₂ (the etch rate and the parameters used are the same as in Section 2.5). Next, the sample was cleaned in acid piranha for 10 minutes.
- After another O₂ plasma surface treatment, a ≈ 100 nm thick layer of SiO₂ solgel (Nanoglass E1200 3:1 in 1-Butanol) [13] was spin-coated and baked for 3 min at

45°C and 2 min at 200°C. This step is repeated three times to reach a thickness of ≈ 375 nm. The latter is obtained by combining an optical thickness measurement (using Filmetrics F20) and a profilometer (KLA – Tencor P7) height scan across the edge of the patterned area (see Fig. 4.7a). Indeed, the degree of planarization obtained with this technique is not global but rather local. As schematically shown in Fig. 4.7b, the solgel thickness h_1 is constant on the bare Al_2O_3 substrate but increases across the edge of the patterned area by Δh . Hence, it is possible to measure h_1 optically with the F20 tool and to extract Δh from the height profile in Fig. 4.7c.

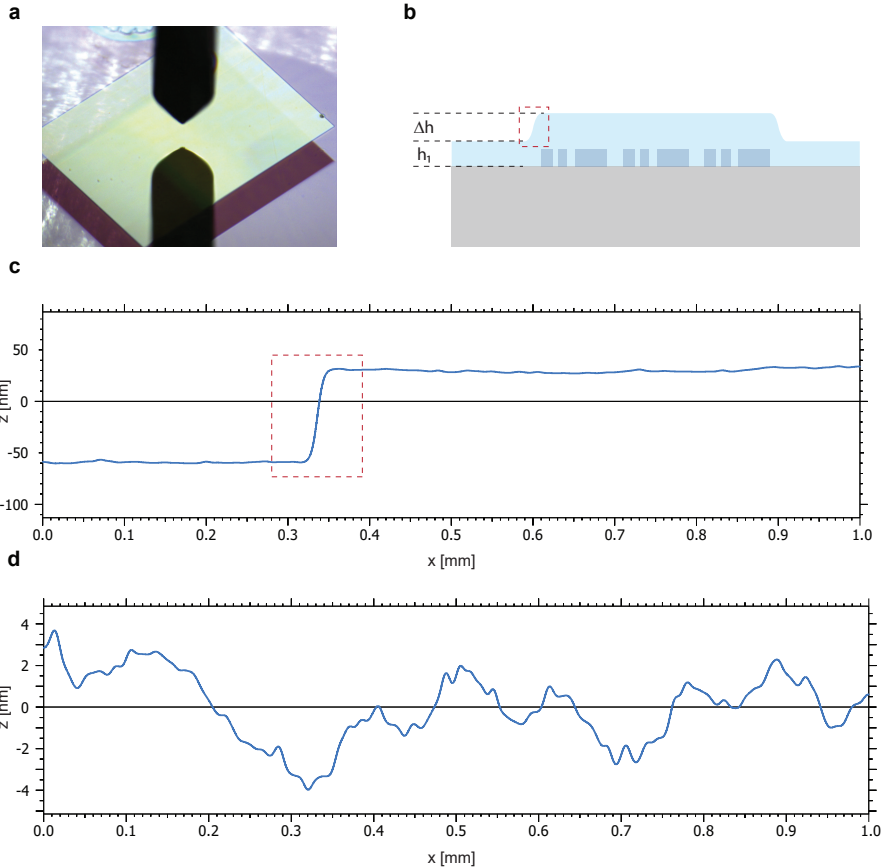


Figure 4.7: **a** Optical image of patterned metagrating area (2×1.5 mm) after solgel planarization. **b** Solgel thickness variation due to local planarization. **c-d** Profilometer height profile scans across the edge of the patterned area (c) and on top of it (d).

- The sample was annealed at 800°C for 10 min. The temperature is ramped up from room temperature to 800°C in 8 min and, after 10 min, ramped down again to room temperature in 5 min. This step serves the purpose of increasing the refrac-

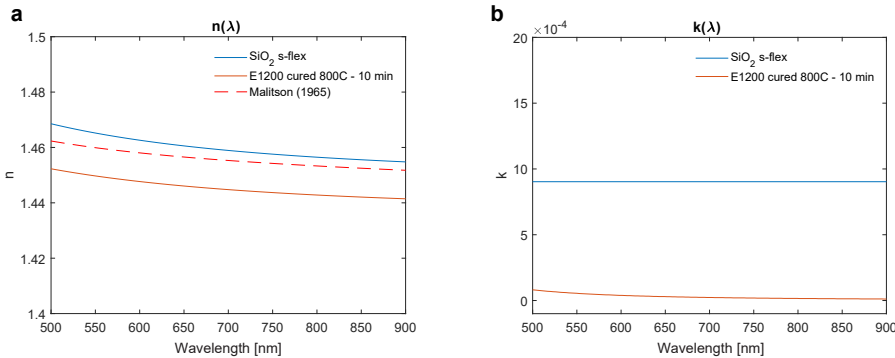


Figure 4.8: Real (a) and imaginary part of the refractive indices of annealed solgel, sputtered SiO₂, and literature values from Ref. [14]

tive index of solgel to values closer to the literature ones used in simulation [14]. Figure 4.8 shows the experimental refractive index values measured via spectroscopic ellipsometry. The SiO₂ thickness is then checked again with Filmetrics F20 and profilometer (KLA – Tencor P7).

- The SiO₂ thickness needed to reach 638 nm is sputtered with Polyteknik Flextura M506 S using a Si source. A clean Si reference sample is also added to the run to check the sputtered SiO₂ thickness and refractive index (see Fig. 4.8). The surface roughness of the final spacer layer on top of the metagrating is evaluated via profilometer height scans (see Fig. 4.7c) and is in the range $0.7 < R_q < 1.6$ nm.
- A 3-aminopropyl trimethoxysilane (APTMS) adhesion monolayer is chemically deposited on the sample [15].
- A 15 nm thick Au layer is evaporated with Polyteknik Flextura M508 E e-beam evaporator. A clean quartz reference sample is also added to the run to check the evaporated Au thickness via transmittance measurements.

4.2.2. CHARACTERIZATION

In this section the sample fabricated following the procedure just described is characterized structurally and optically. As shown in Fig. 4.9, the fabricated structures after the Si reactive ion etching step are uniform and smooth over a large area. Next, it is important to compare the optimized unit cell to the experimental one. Figure 4.10a shows that the etched unit cell follows very closely the optimized contour (red dashed lines in Fig. 4.10a and Fig. 4.3a-b). To corroborate this feature, the transmittance of normal incident light to the 0th diffraction order was measured and compared to its simulated counterpart. In the simulation, the optimized structure described above was used. The transmittance spectrum was acquired over a broad wavelength range ($\lambda_0 = 500\text{--}800$ nm) to obtain maximum sensitivity in the comparison between experiment and simulation. Figure 4.10b demonstrates strong agreement between simulated and measured optical

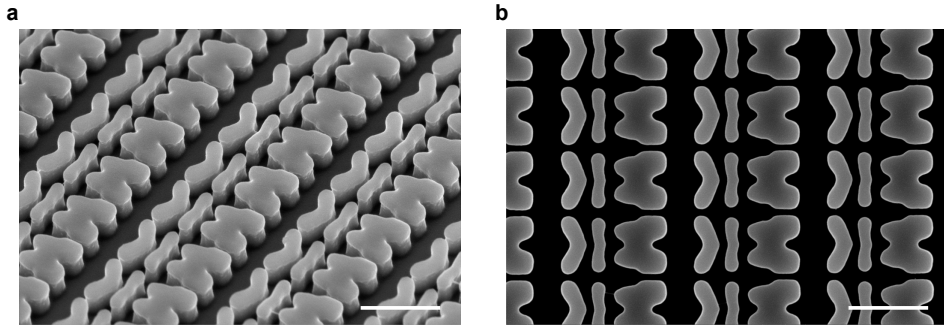


Figure 4.9: **a** Tilted scanning electron microscopy (SEM) image of the patterned Si metagrating. **b** Top-view SEM image of the same patterned area. The scalebar is 500 nm for both panels.

4

spectra, further confirming the suitability of the combined EBL+RIE process to fabricate precisely tailored metagratings for analog optical computing in the visible spectral range.

Next, the cross-section in Fig. 4.10c shows how the SiO_2 spacer conformally embeds the metagrating with no detectable air inclusions, creating a smooth planar top surface. The final thickness of the layer with the embedded metagrating amounts to 638 nm. Again, the transmittance is measured at this step, once more experimentally reproducing the key features present in the simulated ideal spectrum (see Fig. 4.10d). The small discrepancies between experiment and simulation in Fig. 4.10b-d can be attributed to minor fabrication imperfections, such as a slight difference in the SiO_2 refractive index between experiment and simulation, and non-perfectly straight Si etching. The data in Fig. 4.10b-d was collected using the integrating sphere setup described in Section 2.6.1. The sample was illuminated with collimated, TE-polarized, white light from a SuperK EXTREME/FIANIUM supercontinuum laser. The 0th order transmitted light was collected by an integrating sphere and sent to the spectrometer through a multimode fiber. Finally, the Au film evaporation concludes the fabrication, providing the metastructure with a semi-transparent mirror, and hence the required feedback system.

The analog solution of Eq.(4.5) is built up inside the spacer layer in the form of a collection of complex wave amplitudes. These values are hard to retrieve in a far-field experiment, hence we compare the spectroscopic power measurements to simulations of the optimized structure in order to verify the correct operation of our metasurface. Figure 4.11 shows the measured transmittance spectra of the fully fabricated metastructure relating to each S-parameter belonging to S_{2T} or, equivalently, the fraction of transmitted light going into each diffraction channel when the metastructure is illuminated through each input channel above the mirror. Specifically, each sub-panel shows the amplitudes squared of the elements belonging to each column of S_{2T} . Note that the input and output angles are changing with the wavelength of illumination according to the grating equation. In order to collect this data, the setup in Fig. 4.12 was used. The illumination is provided by the same SuperK EXTREME/FIANIUM supercontinuum white-light laser that is monochromated (2 nm bandwidth) by a Laser Line Tunable Filter (LLTF) from Photon Etc. The setup consists of two concentric rotating stages. The

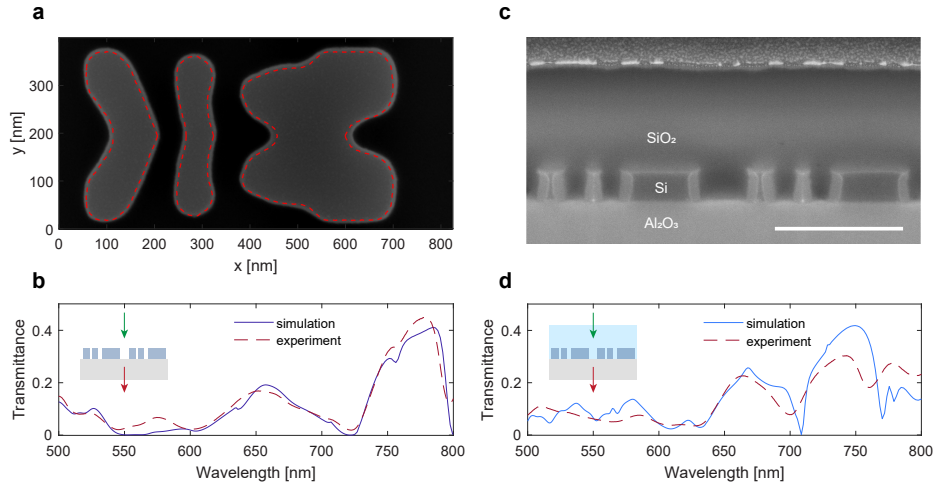


Figure 4.10: **a** Zoomed-in top-view SEM image of a single unit cell compared with the desired optimized contour (red dashed line). **b** Experimental (dashed red) and simulated (dark blue) transmittance spectra of the metagrating after the Si etch step (i.e. without silica spacer and top mirror). The sample was illuminated under normal incidence and the transmitted 0th-order diffraction intensity is collected (inset) as a function of incident wavelength. **c** SEM image of a focused-ion-beam-milled cross-section of the same metagrating embedded in a SiO₂ spacer. **d** Experimental (dashed red) and simulated (blue) transmittance spectra of the metagrating after the SiO₂ planarization step, the scale bar is 500 nm. The input polarization is TE for panels b-d.

sample is mounted on the inner rotating stage (Rot. stage 1 in Fig. 4.12) while an optical power meter (Power meter PM100USB with Photodiode Power Sensor S121C from Thorlabs) is mounted on the outer rotating stage (Rot. stage 2). This configuration allows independent control of θ_0 and θ_T . Light is polarized before impinging on the sample. Each sub-panel in Fig. 4.11 also shows the simulated spectra of the designed ideal metastructure in Fig. 4.5a that gives the solutions shown in Fig. 4.5b. The agreement over a broad wavelength range between simulation and experiment is clear: for each matrix element, the spectral features present in the simulation are reproduced experimentally. Other small discrepancies between experiment and simulation are attributed to minor fabrication imperfections, as described above, that do not hinder the concept of solving an integral equation with the proposed optical-analog scheme. To prove this, Fig. 4.13 shows the robustness of the metagrating based integral equation solver concept against fabrication imperfections. First, the experimental refractive indices of the annealed silica sol-gel and sputtered SiO₂, measured with ellipsometry, are included in the simulations. Next, several unit cell contours are generated from the distribution in Fig. 4.3a by sweeping the binarization threshold (see Fig. 4.13a); this type of fabrication imperfection may arise from unintended resists over- or underexposure. The transmittance corresponding to these slightly eroded and expanded unit cells is simulated and compared to the experimental transmittance data showed in Fig. 4.10b-d. Both for the bare metasurface and for the metasurface including the SiO₂ spacer, the experimental

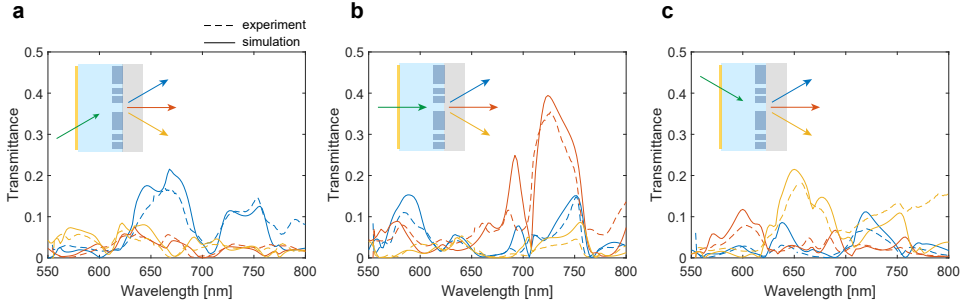


Figure 4.11: **a-c** Experimental (dashed lines) and simulated (solid lines) transmittance spectra of the completed metastructure. Insets: schematic visualization of the metastructure indicating the exciting input port (green arrows) representing orthogonal unit vectors, and the three output ports (yellow, orange, and blue matching the corresponding spectra). The input polarization is TE for all panels.

4

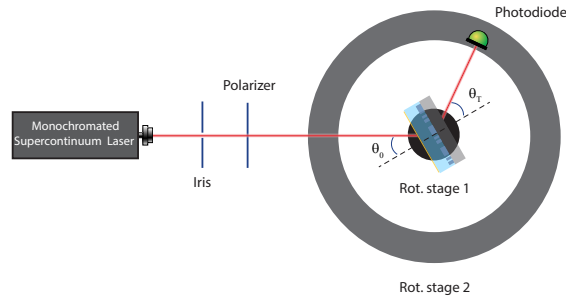


Figure 4.12: Schematics of the setup used to collect the data shown in Fig. 4.11.

data is bounded by the transmittance of an expanded unit cell (level 2.2) and that of an eroded one (level 3.2) being remarkably close to the data of a slightly eroded unit cell (level 2.8). Nonetheless, it is crucial to evaluate the impact of the described imperfections on the performance of the integral solver. For each unit cell the S-matrix was simulated and S_{1R} plotted in Fig. 4.13d-f. The consequence of the mentioned shape distortion is a shift in the operational wavelength. In fact, the minimum distance between the prescribed S-parameters and the simulated ones (i.e. the minimum FOM) is achieved at a different wavelength, which is blue-shifted for the eroded pattern and red-shifted for the expanded counterpart. Also, the FOM value at the minimum depends on the unit cell shape and this has a direct impact on the accuracy of the solution provided by the entire metastructure including the feedback semi-transparent mirror. Figure 4.13 g-i shows how the solution obtained with the three different contours compares to the ideal one. The overall trend is well represented for the different input vectors $(1, 0, 0)^T$, $(0, 1, 0)^T$, $(0, 0, 1)^T$, both in real and imaginary part even for non-ideal designs. Similar results are obtained upon including additional nonidealities such as sloped sidewalls introducing only a small shift in wavelength and a small accuracy loss.

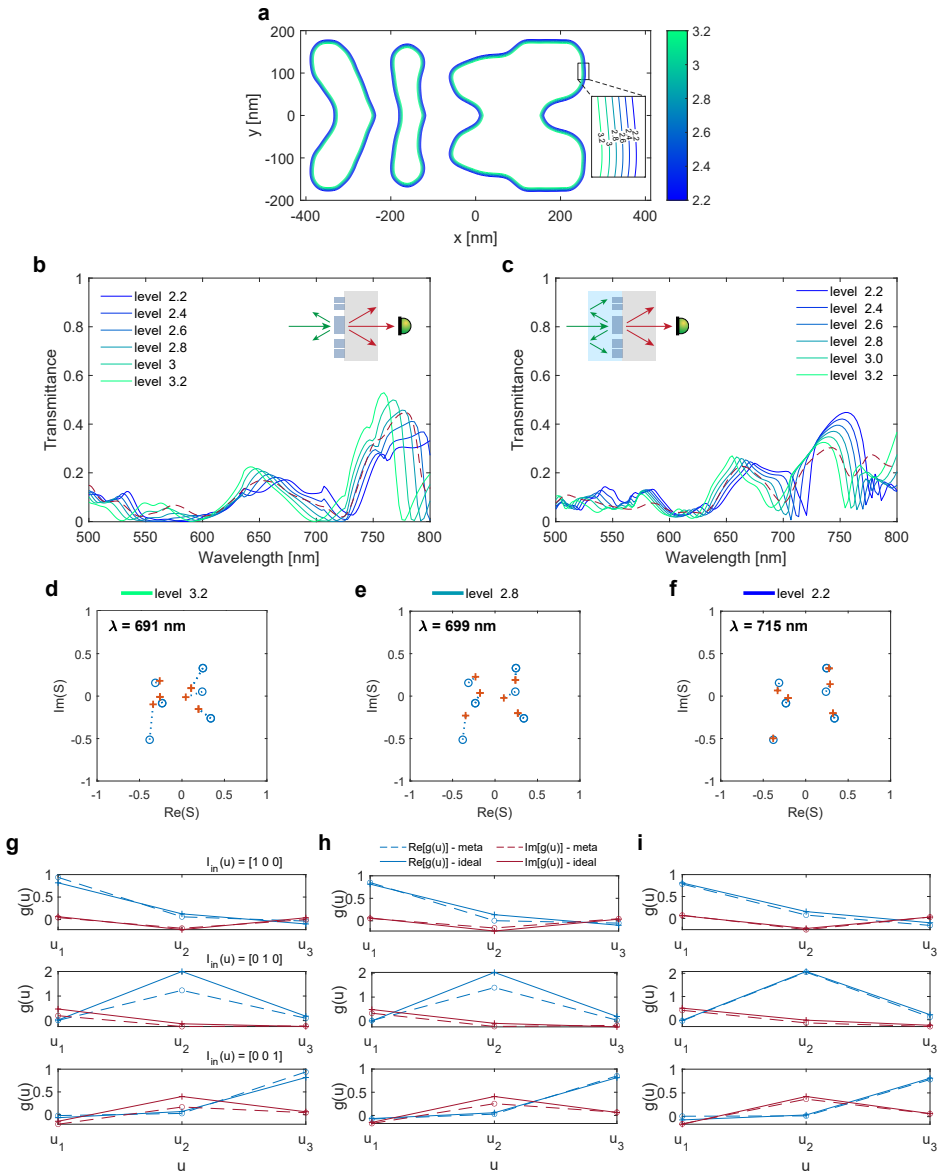


Figure 4.13: **a** Expanded and eroded contours generated from the optimal unit cell refractive index distribution in Fig. S2a. **b** Simulated (solid lines) transmittance spectra (0th transmitted diffraction order) of the metagrating for the contours shown in a. The solid red dashed line is the experimental transmittance also shown in Fig. 4c of the main text. **c** Same as panel b but including the SiO₂ spacer layer. **d-f** Simulated S_{1R} s-matrix sub block for three different unit cell contours (levels 2.2, 2.8, 3.2). **g-i** Comparison between the analog solution obtained from the simulated metastructure transmission and the ideal solution for the same three contours as in d-f and for the three different orthogonal input vectors.

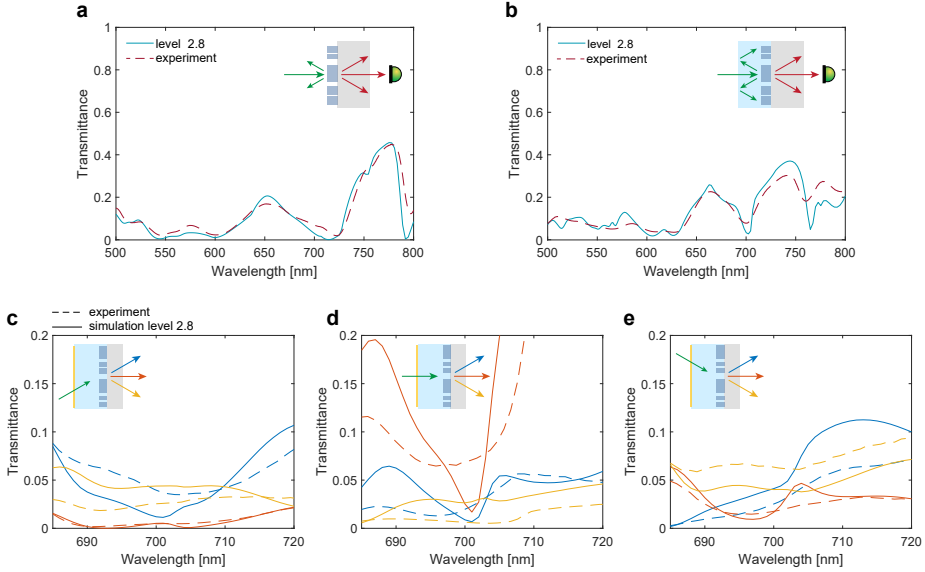


Figure 4.14: **a** Simulated (solid lines) transmittance spectra (0^{th} transmitted diffraction order) of the metagrating for the contour level 2.8. The red dashed line is the experimental transmittance also shown in Fig. 4c of the main text. **b** Same as panel a but including the SiO_2 spacer layer. **c–e** Experimental (dashed lines) and simulated (solid lines - contour level 2.8) transmittance spectra of the completed metastructure. Insets: schematic visualization of the metastructure indicating the exciting input port (green arrows) representing orthogonal unit vectors, and the three output ports (yellow, orange, and blue matching the corresponding spectra).

Next, we can use this fabrication tolerances analysis to benchmark our experimental data and give an estimate of the solution experimentally provided by the metastructure. In fact, it is possible to treat the contour level (i.e. binarization threshold) as a fitting parameter to find the closest matching simulation to the experimental data. Figure 4.14a-b shows the simulated 0^{th} -order transmittance spectra for a slightly eroded unit cell (level 2.8) and its experimental counterpart for the bare metagrating and including the SiO_2 spacer layer. The agreement over a broad wavelength range between simulation and experiment is very good.

Figure 4.14c-e compares the experimental and simulated (contour level 2.8) transmittance spectra of the fully fabricated metastructure relating to each S-parameter belonging to $|S_{2T}|^2$ in a narrower spectral range around the designed wavelength of operation. Again, the experimental spectra reproduce the key features present in the simulated counterpart with rather small deviations. However, in order to validate the use of the simulation with contour level 2.8 as the estimated experimental solution, it is important to assess the impact of such deviations. To do so, we use the generated expanded and eroded designs (contour levels from 2.2 to 3.2) to define a confidence region that bounds our experimental transmittance spectra. Figure 4.15 shows that, even though the experimental data does not correspond perfectly to one specific simulation, at $\lambda = 699 \text{ nm}$ the transmittance lies in the range defined by the simulations with the only exception of the matrix element S_{61} that differs from it by less than 1%. Hence, it

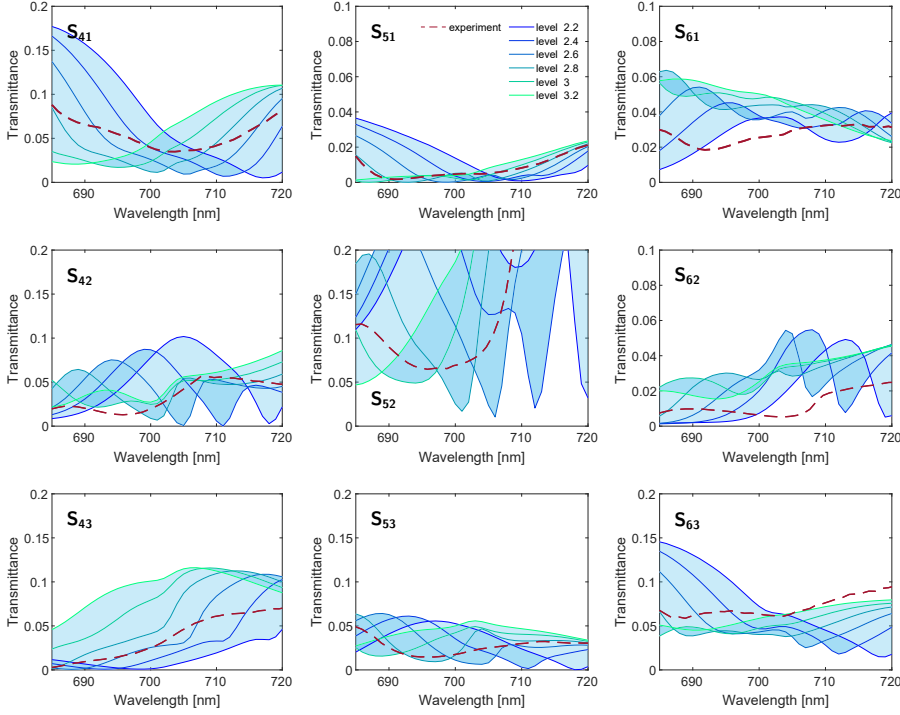


Figure 4.15: **a** Experimental (dashed lines) and simulated (solid lines - contour levels 2.8–3.2) transmittance spectra of the completed metastructure. Each panel corresponds to one element of the matrix S_{2T} .

is possible to select the solution corresponding to contour level 2.8 attributing to it an uncertainty defined by the response of all the other contours at the same wavelength $\lambda = 699$ nm. Figure 4.16 shows the final estimated experimental solution equipped with the latter uncertainty region. The metasurface-based analog solution and the ideal solution show good agreement and similar trends for all the inputs, both in terms of the real and imaginary parts. Furthermore, most of the values corresponding to the ideal solution are compatible with the estimated experimental solution (i.e. lie in its uncertainty region).

While fabrication imperfections have certainly an impact on the overall accuracy, they do not hinder the concept of solving an integral equation with the proposed optical-analog scheme. Moreover, we showed how to retrieve via simulations the solution provided by the metastructure via measuring its response in amplitude in a broad spectral range.

4.3. CONCLUSION

In conclusion, we have presented a Si-based optical metastructure that solves Fredholm integral equations of the second kind in a fully analog fashion at optical frequencies. First, we stated the mathematical problem in terms of the Neumann series successive

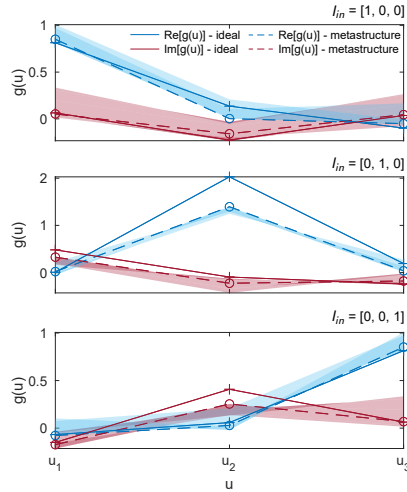


Figure 4.16: Estimated experimental analog solution (real and imaginary parts) of the integral equation (dashed line) compared to the ideal theoretical solution, for the three orthogonal input vectors $(1, 0, 0)^T$, $(0, 1, 0)^T$, $(0, 0, 1)^T$. The wavelength of operation in this simulation is $\lambda = 699$ nm. The shaded regions indicate the uncertainty related to the solution and are generated by the response of several simulations with expanded and eroded designs.

approximation. Next, we discussed the analogy between the integral equation solving and the behavior of an optimized periodic metagrating coupled to a feedback system. At the foundations of this mapping lies the possibility of designing the S-matrix of a periodic structure by setting its periodicity (i.e., the number of input/output modes and hence the dimension of the S-matrix) and optimizing its unit cell (i.e., optimize the coupling of light into the defined diffraction modes in amplitude and phase). Consequently, we show how the designed metastructure effectively solves the problem of interest and compared the metasurface-based solution to the ideal solution. Electron beam lithography and reactive ion etching provide the deep subwavelength spatial resolution required to create a hardware representation of a predefined Kernel, with relatively small deviations between experiment and simulations. We optically characterized the output for different input signals showing good agreement with the ideal simulated response.

Our results demonstrate the possibility of solving complex mathematical problems and a generic matrix inversion at speeds that are far beyond those of the typical digital computing methods. Our solution converges (within 3% difference from the infinite sum) in less than ten passes, corresponding to a processing time of about 20 fs, five orders of magnitude faster than the clock speed of a conventional processor. Operation in the visible spectral range in combination with deep-subwavelength fabrication resolution creates metastructures that are sub-micron thick. This represents a very high degree of circuit integration given the complexity of the mathematical operation performed in this small volume.

Further extensions of this work may explore non-symmetric kernels in a transmissive setup. Also, a similar scheme could be used to estimate the eigenvalues of an inte-

gral operator (a matrix in the discretized form) by exploiting, for example, spontaneous emission of active materials. In fact, this would correspond to the solution of the homogeneous equation corresponding to the Fredholm integral equation of the second kind under study. Moreover, it is possible to scale up the dimensionality of the problem, increasing the number of input/output ports by using more diffraction orders or by encoding information in the polarization state of light. The main challenge in either of these extensions lies in one's ability to accurately fabricate unit cells of higher resolution and smaller feature size required to independently control more degrees of freedom. Of course, a larger number of diffraction orders would imply a larger periodicity and unit cell, partially alleviating this burden. One key advantage of our scheme is the possibility of integrating many designs within a unique feedback system, thus enabling parallelization whenever this is compatible with the problem under study.

Future applications of these concepts could include nonlinear materials within the feedback system (e.g., replacing the SiO₂ spacer layer) to explore nonlinear mathematical problems. Additionally, nonlinearity could also be applied after processing the information via linear operations. Hence, a dedicated external nonlinear device could be designed to process the outputs of our metastructure.

Finally, switchable metagratings (e.g. using phase change materials or mechanical modulation) could be envisioned to dynamically tune the encoded mathematical operation, paving the way for all-optical reconfigurable computing circuitry solving problems of further enhanced complexity.

REFERENCES

- [1] C. Cohen-Tannoudji, B. Diu, and F. Laloe, *An elementary approach to the quantum theory of scattering by a potential*, in *Quantum Mechanics*, Vol. 2 (Wiley).
- [2] G. B. Arfken, H. J. Weber, and F. E. Harris, *Mathematical Methods for Physicists* (Elsevier, 2013).
- [3] N. Mohammadi Estakhri, B. Edwards, and N. Engheta, *Inverse-designed metastructures that solve equations*, *Science* **363**, 1333 (2019).
- [4] M. Camacho, B. Edwards, and N. Engheta, *A single inverse-designed photonic structure that performs parallel computing*, *Nature Communications* **12**, 1466 (2021).
- [5] D. Sell, J. Yang, S. Doshay, R. Yang, and J. A. Fan, *Large-Angle, Multifunctional Meta-gratings Based on Freeform Multimode Geometries*, *Nano Letters* **17**, 3752 (2017).
- [6] T. W. Hughes, M. Minkov, I. A. D. Williamson, and S. Fan, *Adjoint Method and Inverse Design for Nonlinear Nanophotonic Devices*, *ACS Photonics* **5**, 4781 (2018), 1811.01255.
- [7] A. Y. Piggott, J. Petykiewicz, L. Su, and J. Vučković, *Fabrication-constrained nanophotonic inverse design*, *Scientific Reports* **7**, 1786 (2017).
- [8] A. Y. Piggott, J. Lu, K. G. Lagoudakis, J. Petykiewicz, T. M. Babinec, and J. Vucković, *Inverse design and demonstration of a compact and broadband on-chip wavelength demultiplexer*, *Nature Photonics* **9**, 374 (2015).
- [9] S. Molesky, Z. Lin, A. Y. Piggott, W. Jin, J. Vucković, and A. W. Rodriguez, *Inverse design in nanophotonics*, *Nature Photonics* **12**, 659 (2018).
- [10] C. M. Lalau-Keraly, S. Bhargava, O. D. Miller, and E. Yablonovitch, *Adjoint shape optimization applied to electromagnetic design*, *Optics Express* **21**, 21693 (2013).
- [11] G. Rosenblatt, B. Simkhovich, G. Bartal, and M. Orenstein, *Nonmodal Plasmonics: Controlling the Forced Optical Response of Nanostructures*, *Physical Review X* **10**, 011071 (2020).
- [12] L. Li, *Bremmer series, R-matrix propagation algorithm, and numerical modeling of diffraction gratings*, *Journal of the Optical Society of America A* **11**, 2829 (1994).
- [13] M. A. Verschuuren, M. W. Knight, M. Megens, and A. Polman, *Nanoscale spatial limitations of large-area substrate conformal imprint lithography*, *Nanotechnology* **30**, 345301 (2019).
- [14] I. H. Malitson, *Interspecimen comparison of the refractive index of fused silica**, *J. Opt. Soc. Am.* **55**, 1205 (1965).
- [15] J. Sukham, O. Takayama, A. V. Lavrinenko, and R. Malureanu, *High-Quality Ultrathin Gold Layers with an APTMS Adhesion for Optimal Performance of Surface Plasmon Polariton-Based Devices*, *ACS Applied Materials & Interfaces* **9**, 25049 (2017).